

# Chapter 6

## Solid-State NMR Under Ultrafast MAS Rate of 40–120 kHz

Yusuke Nishiyama

**Abstract** With the recent advances in magic-angle spinning (MAS) technology, MAS rates faster than 100 kHz can now be achieved in commercially available probes. The very fast MAS system is comprised of tiny rotors of diameter less than 1 mm, very small sample volume less than 1  $\mu\text{L}$ , very strong rf field strength close to 1 MHz, etc. Because of such extreme features, the very fast MAS measurements require a careful handling of hardware and proper setting of experimental conditions. To this end, the main objective of this chapter is to provide a comprehensive practical guide to set up fundamental experimental conditions (both sample-independent and sample-dependent conditions) associated with very fast MAS technique. The art of shimming, magic-angle adjustment, rf field strength calibration, frequency referencing, repetition delay, and fluctuations in spinning rate are discussed in detail. In addition, two widely used two-dimensional (2D) measurements of  $^1\text{H}$  homonuclear double-quantum/single-quantum (DQ/SQ) correlations and  $^1\text{H}/\text{X}$  cross-polarization heteronuclear single-quantum coherence (CP-HSQC) experiments are introduced.

**Keywords** Fast MAS ·  $^1\text{H}$  indirect detection · Homonuclear correlation  
Heteronuclear correlation

### 6.1 Overview

In general, limited resolution and sensitivity of NMR spectra of solids have always been major roadblocks for widespread applications of solid-state NMR. The presence of orientation-dependent NMR spin anisotropic interactions like chemical shift

---

Y. Nishiyama (✉)  
JEOL RESONANCE Inc., Akishima, Tokyo 196-8558, Japan  
e-mail: yunishiy@jeol.co.jp

Y. Nishiyama  
RIKEN CLST-JEOL Collaboration Center,  
Yokohama, Kanagawa 230-0045, Japan

anisotropy (CSA), dipolar couplings, and quadrupolar couplings, results in broad and featureless NMR spectra of static samples [1, 2]. Magic-angle sample spinning (MAS), which averages out anisotropic interactions to enhance resolution and sensitivity of NMR spectra, serves as an essential technique to study rigid solids [3, 4]. While with the available probe technology the maximum attainable MAS frequency (120 kHz) is larger than the size of the most spin interactions, MAS frequency >120 kHz can still be beneficial in isotopically enriched and naturally abundant chemical, material and biological samples. One of the major advantages of the very fast MAS technique is the reduced broadening of  $^1\text{H}$  NMR resonances due to suppression of  $^1\text{H}$ - $^1\text{H}$  homonuclear dipolar interactions in rigid  $^1\text{H}$  networks, which is inversely proportional to the sample spinning frequency [5, 6]. Consequently, a combination of the very fast MAS, high natural abundance, and high sensitivity of protons allows the  $^1\text{H}$  indirect observation of X nuclei with enhanced sensitivity [7–16]. The application of very fast MAS to the systems with large anisotropies like quadrupolar nuclei, heavy spin-1/2 nuclei, paramagnetic systems is shown to be very efficient for their structural characterization by several research groups [17–23]. Many excellent review articles on very fast MAS NMR technique can be found in the literature that introduce the engineering improvement, giving the theoretical backgrounds and discussing the practical applications [5, 24–35]. However, it is not straightforward to use very fast MAS techniques especially for researchers with non-NMR background. In this regard, the purpose of this chapter is not to provide a comprehensive review of the very fast MAS technique, rather to introduce the practical hands-on guide to researchers using this technique for structural and dynamics studies of rigid solid samples.

The very fast MAS probes with a diameter of 0.7–2 mm have several advantages and disadvantages over the commonly used slow to moderate MAS systems with a diameter of 3–5 mm. Advantages are (a1) faster MAS rate [36–47], (a2) smaller sample volume, (a3) stronger rf field strength with the same rf input, (a4) high sensitivity per unit volume, (a5) smaller temperature increase due to friction loss at the same MAS rate, (a6) use of low power sequences [48–52], and (a7) less E-field heating for lossy samples. The disadvantages are (d1) lower absolute sensitivities at the same experimental conditions, (d2) difficulty in sample and probe handling, (d3) limited temperature range, and (d4) generally more expensive. It is crucial to choose the appropriate sample rotors depending on the system of interest, considering the above-mentioned advantages and disadvantages. Nowadays, the probes with a capability of MAS rate faster than 100 kHz are commercially available (a1). Since the spinning frequency is typically limited by the speed at the surface which is close to the speed of sound at the maximum attainable MAS rate, the practical solution to achieve faster MAS is to make the sample rotor smaller. This accompanies with the small sample volume (a2). The very fast MAS probe for 100+ kHz MAS rate needs the rotor diameter of 0.7–0.75 mm with the sample volume less than 0.5  $\mu\text{L}$ , which is hundred times smaller than that of standard MAS rotor (ca 50  $\mu\text{L}$  for 4 mm). Although the tiny sample volume accompanies with the limited absolute sensitivity, the capability of volume limited sample analysis dramatically reduces the barrier to prepare and analyze costly samples such as fully isotopically labeled protein

samples, natural products, tissues samples. Moreover, the smaller diameter allows the micro-sized sample coil. This achieves the high  $B_1$  field with a given rf field input to the probe (a3). Such characteristics of the probe design is particularly useful to reduce the rf input for given  $B_1$  field and to maximize the  $B_1$  field to excite broad spectral range of quadrupolar nuclei, heavy spin-1/2 nuclei, paramagnetic samples, etc. For example, the rf field strength for  $^1\text{H}$  can be close to 1 MHz at 100 W input. From the reciprocal relationship, the sensitivity from a given induced  $B_1$  field is maximized (a4). This maximizes the sensitivity if the available sample amount is limited. In addition, speed at the surface is proportional to the diameter of sample rotor. This reduces the friction heating at a given MAS frequency (a5). At the MAS frequency >40 kHz, the most spin interactions are averaged out because the size of most spin interactions is smaller than the MAS frequency. This changes the spin dynamics dramatically and allows the use of the so-called low power sequences like decoupling, recoupling, cross-polarization (CP) (a6). This is particularly beneficial to heat-sensitive samples like biomolecules with the additional advantage of less friction heating (a5) and high rf efficiency (a3). It is also important to note that low power sequences like decoupling at very fast MAS reduces the complexity in setting up experiments in comparison with their counterparts at slow MAS that require high-power rf pulses. Therefore, an extra care should be taken to avoid any damage to the probe while setting such experiments at slow MAS. On the other hand, the limited sample volume is problematic due to the low sensitivity (d1) of the NMR spectra. Therefore, the measurements using moderate or large rotors are advisable if very fast MAS rate is not required and the available sample volume is enough to fill these larger rotors. In addition, the sample packing for the very fast MAS probe takes much longer time (typically 10–30 min) than the standard rotor, potentially reducing the overall throughput (d2). Since the operating temperature range of very fast MAS probes is limited (typically  $-50$  to  $+50$  °C) compared to the conventional MAS systems (typically  $-100$  to  $200$  °C), the range of sample temperature is also limited (d3). The initial and maintenance cost, including rotors, caps, consumables, of very fast MAS probes is typically more expensive than those of the conventional MAS probes (d4), and therefore, only selected laboratories across the world have privilege to such facilities.

On the basis of our own experiences at our research laboratory, we will introduce the practical setup of experimental conditions at very fast MAS rate in this chapter. While the basic setup is the same as the standard MAS systems, there are several points which one should take care under the very fast MAS conditions. The following sections highlight the practical aspects of very fast MAS experiments. First, we focus on the basic setup of very fast MAS probes, including magic-angle adjustment, shimming, referencing, and rf field calibration. These setups are not sample dependent and can be adjusted using standard samples whenever one starts very fast MAS experiments. The sample-dependent optimizations of repetition delay and hardware handlings are also summarized. Finally, basic 2D experiments,  $^1\text{H}$  double-quantum (DQ)/single-quantum (SQ) correlations and  $^1\text{H}$ -detected cross-polarization heteronuclear single-quantum coherence (CP-HSQC) measurements are introduced.

## 6.2 Setup of Sample-independent Factors

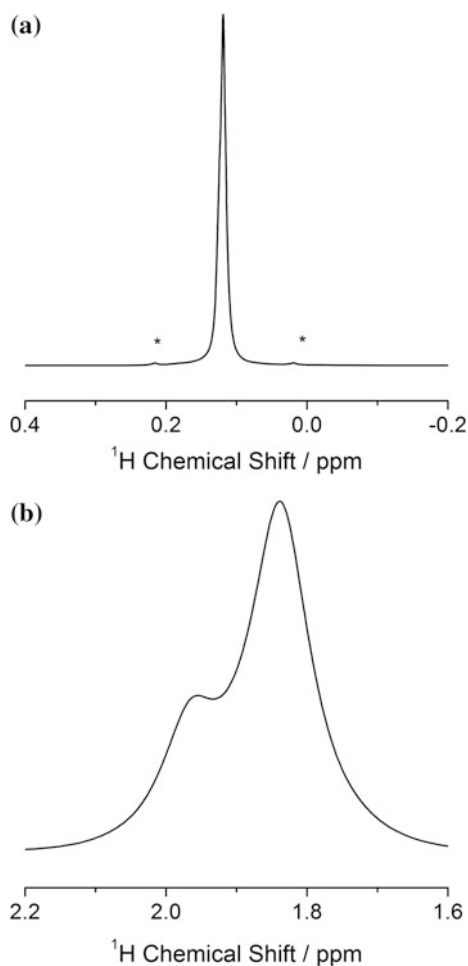
### 6.2.1 *Shimming*

Homogeneous static magnetic field is crucial for all the high-resolution NMR experiments. Since the NMR lines are usually broad in rigid solids, the contributions to the line broadening from the inhomogeneous static field were considered to be insignificant in the past. However, such effects now can no longer be treated as insignificant due to recent developments of probe technology and methods to achieve high resolution in solid-state NMR including  $^1\text{H}$  NMR at very fast MAS. The field variations are adjusted by the corrective magnetic fields. In the modern NMR spectrometer, it is achieved by additional electromagnets, i.e., shim coils [53]. The source of inhomogeneity comes from both sample-independent factors, including inhomogeneity from the main magnet, effect of probe components, and sample-dependent factors, including magnetic susceptibility broadening. Therefore, the shim-coil current basically must be optimized for sample to sample. In the solution NMR, the shim values can be automatically adjusted by the field gradient methods [54–56], which allow optimization within minutes for every sample. On the other hand, the susceptibility broadening in solid-state NMR is largely suppressed by MAS in solid-state NMR [57–59]. This avoids the need to optimize shim values sample to sample and the same shim values can be retained for all the samples. The automatic shimming in MAS NMR is recently introduced using the field gradient produced by the shim coil [60]. However, these field gradients are not sufficiently strong enough to apply to short samples used in very fast MAS experiments. Thus, the fast MAS probe still requires manual shimming to achieve high resolution.

In the solution NMR, shimming can be done by changing the values along  $z$ -axis including,  $Z1$ ,  $Z2$ ,  $Z3$ . This is because the inhomogeneity along the  $x$ - and  $y$ -axes is averaged by sample spinning along the  $z$ -axis and only results in spinning sidebands. In the solid-state NMR, the axis of sample spinning is different from that of solution NMR, making different set of shim terms effective [61, 62]. Assuming the axis of sample spinning lies in the  $YZ$  plane, the first-order shimming can be done by  $Z1$  and  $Y1$  and the second-order by  $YZ$  and  $X2$ – $Y2$  ( $X2$ ). It should be noted that  $Z2$  does not give any effect on lineshape. Generally,  $Z1$  is more efficient than  $Y1$ ; thus, we can safely use  $Z1$  for the first-order shimming. However, if  $Z1$  is not strong enough,  $Y1$  can additionally be used. Since the two bearings are located at the both end of the sample rotors, large second-order terms are required. Typically either  $YZ$  or  $X2$ – $Y2$  alone is not sufficiently strong enough. The combined use of these two terms is recommended. It should be noted that care must be taken on the sign of  $YZ$  and  $X2$ – $Y2$  terms, otherwise  $YZ$  and  $X2$ – $Y2$  may cancel out each other. Usually, the first- and second-order terms are enough to obtain sufficient resolution. The orthogonal field inhomogeneity with respect to sample spinning axis can be neglected because of the very fast MAS rate.

The manual shimming is typically done by monitoring NMR signal lineshape. Adamantane is commonly used for shimming by monitoring  $^{13}\text{C}$  (CP)MAS lineshape for the most solid-state NMR setup. However, the very fast MAS probe requires the other sample for shimming because of its limited sensitivity.  $^1\text{H}$  NMR spectrum of a piece of silicone rubber wherein molecular motions mostly average out anisotropic interactions is useful for shimming because of high resolution and sensitivity in the presence of very slow MAS (2–5 kHz). Even much faster MAS can also be used without any harmful effects. The  $^1\text{H}$  NMR spectra of silicone rubber at 20 kHz MAS is shown in Fig. 6.1a. The shimming should be done to minimize not only the full width at half maxima but also the width at the foot of the peak. The  $^1\text{H}$  NMR linewidth at half maxima is 0.011 ppm and at 0.55% is 0.1 ppm for silicone rubber. Alternatively,  $^1\text{H}$  NMR of adamantane can be used (Fig. 6.1b at 80 kHz MAS). Because of intermolecular  $^1\text{H}$ – $^1\text{H}$  dipolar interaction, faster MAS

**Fig. 6.1** **a**  $^1\text{H}$  NMR spectra of silicone rubber under 20 kHz MAS and **b** adamantane under 80 kHz MAS. The spectra were measured at 14.1 T. Asterisks (\*) in (a) indicate the carbon satellites

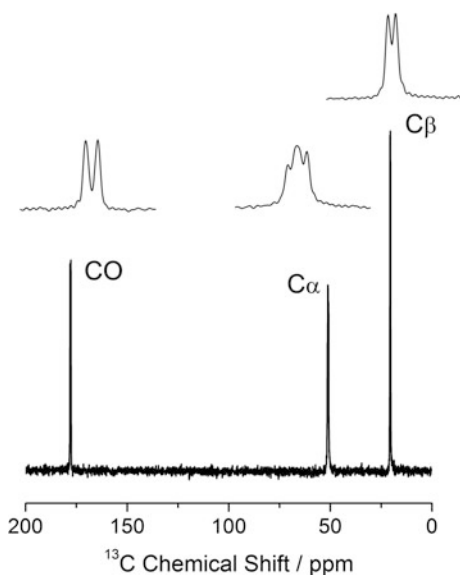


>80 kHz is required for this case, where  $^1\text{H}$  NMR of CH and  $\text{CH}_2$  starts to be resolved. In addition, the magic angle should be adjusted. Thus, iterative adjustment is required between shimming and magic-angle adjustment for adamantane.

## 6.2.2 Magic-Angle Adjustment

The precise magic-angle adjustment is required for all the MAS NMR experiments. The satellite transitions of  $^{79}\text{Br}$  of KBr are widely used to adjust magic angle at a MAS frequency of 5–10 kHz [63]. Following the similar approach, the magic angle in the very fast MAS probes can be adjusted by using  $^{27}\text{Al}$  of simple compounds like kaolin. Alternatively,  $^{13}\text{C}_3$ ,  $^{15}\text{N}$  L-alanine can be used for the precise magic-angle adjustment. The  $^{13}\text{C}$  CPMAS peaks are resolved by  $^{13}\text{C}$ – $^{13}\text{C}$  homonuclear J-coupling and immune to  $^{13}\text{C}$ – $^{13}\text{C}$  homonuclear dipolar interactions at the MAS frequency >30 kHz [20]. The CO carbon, which shows large  $^{13}\text{C}$  CSA, gives lineshape, which is very sensitive to the magic angle. Thus, the magic angle can be precisely adjusted by maximizing the depth of splittings of the CO peak. While the splitting comes from homonuclear J-interactions (ca. 55 Hz), which is immune to the magic angle, the line broadening due to residual CSA is very sensitive to the magic angle. Thus, the depth of the splitting gives good measure of the magic angle. The spectra after MAS adjustment are shown in Fig. 6.2. It should be noted that this splitting is also sensitive to shim, and therefore, iterative optimization of shimming and magic-angle adjustment is required for getting the best output. The other carbons also show splitting but are much less sensitive to magic angle.

**Fig. 6.2**  $^{13}\text{C}$  CPMAS spectrum of  $^{13}\text{C}_3$ ,  $^{15}\text{N}$  L-alanine measured at 14.1 T under 70 kHz MAS. *Insets* are expansion of each peak with a spectral width of 4 ppm. While  $^{13}\text{C}$ – $^{13}\text{C}$  J-couplings give major splittings, the  $^{15}\text{N}$ – $^{13}\text{C}$  J-coupling also affects the splitting of the  $\text{C}\alpha$  carbon signal

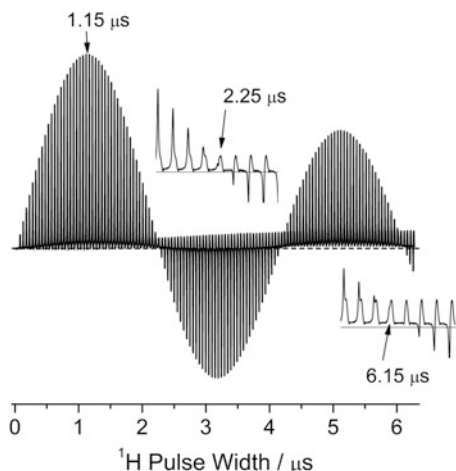


### 6.2.3 *rf Field Strength Calibration*

The rf magnetic field strength ( $B_1$ ) calibration is one of the fundamental adjustments in experimental NMR setup. It can be usually measured by the nutation curve (mostly sinusoidal), which is a set of single-pulse NMR spectra recorded with varying the excitation pulse width. The  $90^\circ$  and  $180^\circ$  pulse width can be measured from the first maxima and null point, respectively. The rf field strength is calculated from either  $90^\circ$  or  $180^\circ$  pulse width. However, such procedure may result in some error in the rf field strength estimation due to rf transients (amplitude and phase) in very fast MAS probes. The amplitude and phase transients are created at the rising and falling edges of the pulses in high-Q NMR probes and can be significant in very short pulses. As a result, noticeable elongation of  $90^\circ$  and  $180^\circ$  pulse widths is observed, which is reflective of error in the calculated rf field strength. To avoid such complexities, nutation curve up to a pulse width  $540^\circ$  is recommended in the pulse width calibration measurement; i.e., nutation curve should at least have three null points. The  $90^\circ$  and  $180^\circ$  pulse widths are determined from the first maxima and null point, respectively. These values already include the effect of pulse transients, and, thus, can safely be used for  $90^\circ$  and  $180^\circ$  pulses. The difference between  $540^\circ$  and  $180^\circ$  pulse widths removes the effect of pulse transient effects, allowing the estimation of rf field strength in continuous irradiations. This value can be safely used to set up the continuous or semi-continuous rf irradiations, including decoupling/recoupling sequences, CP.

The  $^1\text{H}$  rf field calibration can be done by any sample containing hydrogen. An example of nutation curves is shown in Fig. 6.3 using  $^{13}\text{C}_3, ^{15}\text{N}$  L-alanine. The repetition delay should be sufficiently ( $\sim$ three times) longer than  $^1\text{H}$   $T_1$  relaxation time. Shorter repetition time shifts the first maxima toward shorter length, resulting in underestimation of  $90^\circ$  pulse width, while the position of null points is immune to the repetition delay. Thus,  $180^\circ$  pulse width, which is determined by the first null point, can be used for rough estimation of rf field strength even with shorter repetition delays. Since this phenomenon occurs due to the residual magnetization from the previous scans, instead of long repetition delay, saturation pulses to suppress the residual magnetization just before the repetition delay can be used with the cost of low sensitivity. Care must be taken when the null point is evaluated; the null points should be taken from the pulse length where the signal intensity from the sample is minimized with respect to the background signal rather than where the signal intensity becomes zero. Figure 6.3 shows visible background signals, and the narrow hump and the broad baseline originating from signals from caps and static component (MAS stator, capacitor, etc.), respectively. Since background signals feel much weaker rf field strength than that from the sample, these signals keep growing with increase in the pulse width. This results in deviation of baseline from zero-intensity line (shown as dotted line in Fig. 6.3). If null point is taken from the position where the signal intensities are zero, the signal is already negative compared to the baseline, overestimating the  $180^\circ$  and  $540^\circ$  pulse lengths. In the present case, the  $90^\circ$ ,  $180^\circ$ , and  $540^\circ$  can be measured as 1.15, 2.25, and 6.15  $\mu\text{s}$ ,

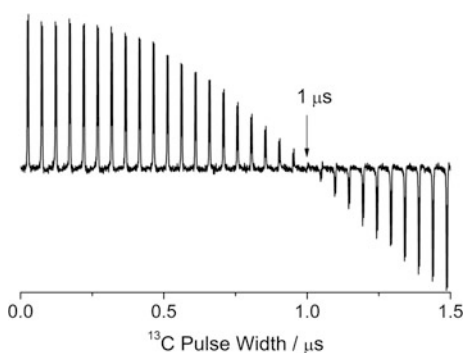
**Fig. 6.3**  $^1\text{H}$  nutation curve of the  $\text{NH}_3^+$  signal of  $^{13}\text{C}_3$ ,  $^{15}\text{N}$  L-alanine at 70 kHz. The insets are expansion around  $180^\circ$  and  $540^\circ$  pulses (first and third null point). The zero-intensity line is shown by the dotted line



respectively. The rf field strength for CW irradiations can be obtained as  $1/(6.15 - 2.25 \mu\text{s}) = 256 \text{ kHz}$ . The calculated  $180^\circ$  and  $540^\circ$  pulses can be expected to be two and six times longer than  $90^\circ$  pulse, respectively, and, however, are shorter than observed from the nutation curve. In the other words, the observed  $90^\circ$  and  $180^\circ$  pulse lengths are longer than those expected from the rf field strength (0.98 and 1.95  $\mu\text{s}$ ). This is because the pulse transients elongate the observed  $90^\circ$  and  $180^\circ$  pulse widths. Moreover, long rf irradiation selects the homogeneous  $B_1$  field region, which typically gives the stronger rf field.

In a similar way, the  $^{13}\text{C}$  rf field strength can also be measured.  $^{13}\text{C}_3$ ,  $^{15}\text{N}$  L-alanine is useful sample because of short  $T_1$  relaxation time of  $\text{CH}_3$ . Instead,  $^{13}\text{C}$  CPMAS experiments with additional  $^{13}\text{C}$  pulse right after the CP can be used to overcome the long  $^{13}\text{C}$   $T_1$  relaxation time. This results in cosine sinusoidal curve and  $90^\circ$  pulse width can be obtained from the first null point (Fig. 6.4).

**Fig. 6.4**  $^{13}\text{C}$  cosine nutation curve observed by  $^{13}\text{C}$  CPMAS with the additional  $^{13}\text{C}$  pulse with various pulse lengths right after CP. CO signal of  $^{13}\text{C}_3$ ,  $^{15}\text{N}$  L-alanine at 14.1 T under 70 kHz MAS is plotted





In the very fast MAS experiments, wide range of rf field strengths is required for recoupling and decoupling interactions. In addition, shaped pulses also require various rf field outputs. It is very time-consuming process to calibrate the wide variety for rf field strength. Fortunately, the modern NMR spectrometers are equipped with very high linear amplifiers and some spectrometers have calibration table to compensate the residual nonlinear responses of high-power amplifiers. This avoids the need of rf field strength calibration at various output levels. Instead, the calculated value from a certain rf-output level can safely be used.

## 6.2.4 Reference

The solid-state NMR spectra can be referenced by the external reference, because shift in peak position is not expected from one sample to another unlike solution NMR. The useful reference material should have the following characteristics: (1) sharp lineshape, (2) less temperature dependence, (3) fine powder, (4) short  $T_1$  relaxation time, (5) high sensitivity, and (6) non toxic. The list of standard samples for  $^1\text{H}$ ,  $^{13}\text{C}$ , and  $^{15}\text{N}$  secondary references are listed in Table 6.1. For the practical use, we recommend  $^{13}\text{C}_3$ ,  $^{15}\text{N}$  L-alanine because it can be used for multiple purpose including magic-angle adjustment, CP setup, rf field calibrations. However, the linewidths of  $^{13}\text{C}_3$ ,  $^{15}\text{N}$  L-alanine are somewhat broad; thus, the other samples can be useful for fine referencing.

**Table 6.1** List of samples for peak shift reference

Nucleus	Sample	Shift (ppm)
$^1\text{H}^{\text{a}}$	Silicone rubber	0.119 [64]
	Adamantane (CH)	1.84
	Adamantane (CH <sub>2</sub> )	1.95
	$^{13}\text{C}_3$ , $^{15}\text{N}$ L-alanine (CH <sub>3</sub> )	1.5
	$^{13}\text{C}_3$ , $^{15}\text{N}$ L-alanine (CH)	3.9
	$^{13}\text{C}_3$ , $^{15}\text{N}$ L-alanine (NH <sub>3</sub> <sup>+</sup> )	8.6
$^{15}\text{N}^{\text{b}}$	NH <sub>4</sub> Cl	39.3 [65]
	$^{13}\text{C}_3$ , $^{15}\text{N}$ L-alanine	42.7
$^{13}\text{C}^{\text{c}}$	Adamantane (CH)	29.45 [66]
	$^{13}\text{C}_3$ , $^{15}\text{N}$ L-alanine (CH <sub>3</sub> )	20.55 <sup>d</sup>
	$^{13}\text{C}_3$ , $^{15}\text{N}$ L-alanine (CH)	51.11 <sup>d</sup>
	$^{13}\text{C}_3$ , $^{15}\text{N}$ L-alanine (COOH)	177.88 <sup>d</sup>

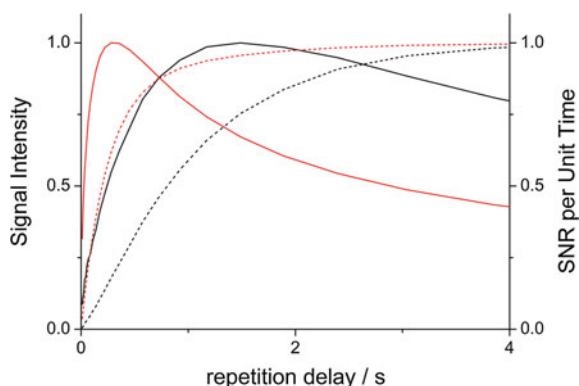
With respect to <sup>a</sup>TMS, <sup>b</sup>liquid NH<sub>3</sub>, and <sup>c</sup>TMS, <sup>d</sup>peak positions are calculated at the center of gravities of the peaks

## 6.3 Sample-Dependent Setup

### 6.3.1 Relaxation Delay

For time-effective NMR measurements, it is crucial to optimize the relaxation delay, or an idle time between the consecutive scans to relax the spin system toward its thermal equilibrium state. The signal intensity per scan is maximized when spins achieve the Boltzmann distribution at thermal equilibrium; however, the number of scans per unit time is minimized at the same time, leading to low signal to noise ratio (SNR) per unit time. Each scan includes (a) noise—a random process whose magnitude is constant for every scans, and (b) signal—whose magnitude depends on the repetition delay. Therefore, the SNR per unit time heavily relies on repetition delay. Assuming the mono-exponential relaxation, the SNR is maximized when the repetition delay is equal to 1.26 times of  $T_1$  relaxation time. Since the SNR per unit time drops very rapidly when the repetition delay is shorter than its optimal value, it is recommended to use slightly longer repetition time than the theoretical maximum. 1.5–2 times of the  $T_1$  relaxation time can be good compromise between the time efficiency and any underestimation of the  $T_1$  relaxation time. The  $T_1$  relaxation can be measured either by the saturation or inversion recovery methods. The inversion recovery measurements give higher sensitivity, thus better accuracy, than saturation recovery because the signal intensity varies from  $-M$  to  $+M$  for former on the other hand from 0 to  $+M$  for latter. However, the relaxation delay should be longer than 3–5 times of  $T_1$  relaxation time in inversion recovery experiments, since the spin systems should be close to the thermal equilibrium before each scan. This complicates the setup of inversion recovery experiments, since the  $T_1$  relaxation time is not known before measurements. In practical use, saturation recovery is recommended because the repetition delay can be set to zero or very short value regardless of the  $T_1$  relaxation time. The  $T_1$  relaxation sometimes does not follow the single exponential curve, making 1.26 times rule ineffective. In such a case, application of  $\sqrt{\tau}$  window function is advisable, where  $\tau$  denotes the recovery duration between the saturation pulses and the read pulse. This window function gives SNR per unit time as a signal intensity in saturation recovery curve. Of course, it can be applied to mono-exponential curve as well, giving maxima at 1.26 times of the  $T_1$  relaxation time (Fig. 6.5). Moreover, the  $\sqrt{\tau}$  window function can be used not only for saturation recovery but also for any other sequence with varying repetition delay, wherever the pulse schemes saturate magnetization after the measurements. This is particularly useful when only a part of NMR signal contributes to the final results. For example, in the  $^1\text{H} \rightarrow ^{13}\text{C} \rightarrow ^1\text{H}$  filtering experiments, the appropriate repetition delay should be determined by the recovery curve of  $^1\text{H}$ , which is directly attached to  $^{13}\text{C}$ . However, it is not straightforward to monitor the recovery curve of  $^1\text{H}(-^{13}\text{C})$ , since the  $^1\text{H}(-^{13}\text{C})$  signals are buried with the  $^1\text{H}$  signals, which are connected to  $^{12}\text{C}$  in the samples at natural abundance.

**Fig. 6.5**  $^1\text{H}$  saturation recovery curves with (solid) and without (dotted)  $\sqrt{\tau}$  window function of  $\text{NH}_3^+$  (red) and  $\text{CH}_2$  (black) signals of  $\alpha$ -glycine at 70 kHz MAS under 14.1 T. The mono-exponential curve fitting gives the  $^1\text{H}$   $T_1$  relaxation times of 0.32 s for  $\text{NH}_3^+$  and 1.0 s for  $\text{CH}_2$



Moreover, the  $T_1$  relaxation time between these  $^1\text{H}$ s can be different because of presence/absence of  $^{13}\text{C}$  neighbor. It should be noted that the combination of the  $\sqrt{\tau}$  window function and actual pulse sequences like  $^1\text{H} \rightarrow ^{13}\text{C} \rightarrow ^1\text{H}$  filtering experiments requires enough number of prescans since it is assumed that the system reaches to the steady state.

The  $^1\text{H}$   $T_1$  relaxation time is assumed to be uniform at the moderate MAS rate because of rapid spin diffusion among  $^1\text{H}$ s, which smears the difference of intrinsic  $^1\text{H}$   $T_1$  relaxation time. However, the very fast MAS slows down the spin diffusion, reintroducing the variation of  $^1\text{H}$   $T_1$  [67]. It is also illustrated in Fig. 6.5;  $\text{NH}_3^+$  and  $\text{CH}_2$  protons of  $\alpha$ -glycine give different recovery behaviors in saturation recovery experiments. These phenomena are frequently observed at the very fast MAS rate and can be problematic to set up optimal repetition delay, especially if the peak of interest has long  $T_1$  relaxation time than that of the other  $^1\text{H}$ s. For example, the  $T_1$  relaxation time of  $^1\text{H}$ s among the same molecule can vary from several to hundreds seconds at the very fast MAS rate. To overcome this problem,  $^1\text{H}$ - $^1\text{H}$  spin diffusion can be turned on during the repetition delay by applying rf driven recoupling (RFDR) schemes shown in Fig. 6.6 [68, 69]. RFDR transfers the magnetization from the rapidly relaxing components to slow relaxing components, utilizing rapid relaxation mechanism several times between consecutive scans. It should also be noted that the efficiency depends on the phase cycling (Fig. 6.7). The optimization can be done by (1) optimization of integer  $m$  and  $n$  shown in Fig. 6.6, and (2) optimization of repetition delay using the  $\sqrt{\tau}$  function with saturation recovery schemes. The optimization should be repeated iteratively until convergence. The initial  $\tau$  can be determined by the optimal repetition delay for the shortest  $T_1$  component. This sensitivity enhancement is particularly useful for NH and OH measurements, which are typically isolated from the other  $^1\text{H}$ s and tend to show longer  $T_1$  relaxation time.

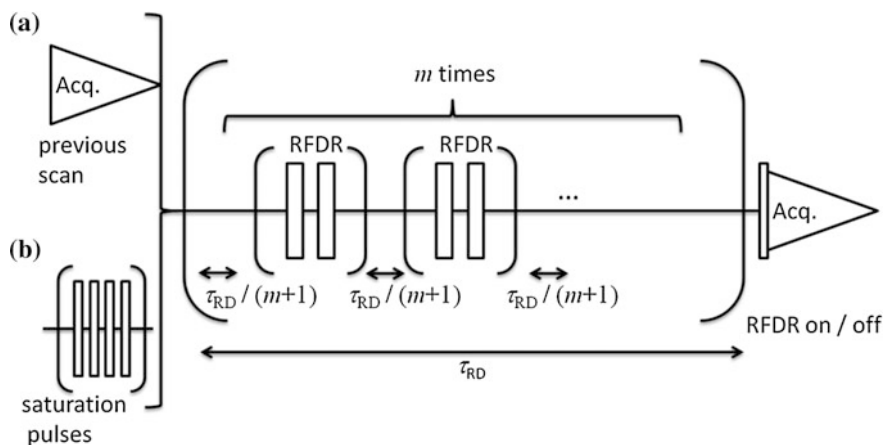


**Fig. 6.6** Pulse schemes used in the **a** general experiments and **b** saturation recovery experiments. The equally spaced  $m$  RFDR trains can be applied during  $\tau_{RD}$ . While  $\pi/2$  pulse is applied just before the acquisition in the single-pulse experiments and saturation recovery experiments, any pulse scheme can be applied after  $\tau_{RD}$  delay. Reproduced from Ref. [69] with permission from Elsevier

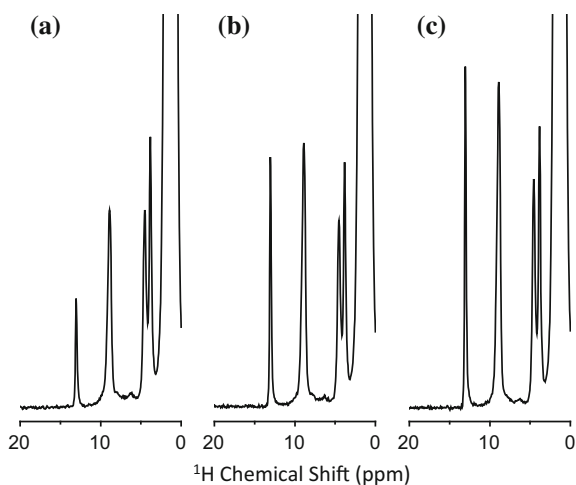


**Fig. 6.7** Single-pulse  $^1\text{H}$  NMR spectra of a powder  $N$ -acetyl- $^{15}\text{N}$ -L-valyl- $^{15}\text{N}$ -L leucine (NAVL) sample obtained at 100 kHz MAS without fp-RFDR (**a**), with fp-RFDR of  $(\text{XY}8)_4^1$  (**b**), and with fp-RFDR of  $(\text{XY}4)_4^1$  (**c**) during the recycle delay. A relaxation delay of 2.2 s and rf field strength of 467 kHz for fp-RFDR were used. Number of fp-RFDR cycles (3 for **b** and 6 for **c**) and duration of each fp-RFDR (1.92 ms for **b** and 6.4 ms for **c**) were optimized such that the carbonyl proton peak (13 ppm) is maximized. Reproduced from Ref. [70] with permission from Elsevier

### 6.3.2 Hardware Treatment

Since the very fast MAS probe consists of very precise micro-engineering parts, contamination with very tiny dust particles, lint, even moisture causes fatal crush. Thus, the maximum attention should be paid to avoid this by following the procedure written each instruction manual. The same level of attention should be paid for sample packing as well.

Here, we discuss the stability of MAS. Some of recoupling sequences need two separated rf irradiations synchronous to sample spinning. One example can be seen in D-HMQC experiments [70, 71], which are widely used in  $^1\text{H}$ - $^{14}\text{N}$  correlation measurements [72–74] at the very fast MAS conditions. The other example can be found in  $^1\text{H}$  DQ/SQ correlation experiments (see Sec.6 4.1). The synchronization can be done by either calculating the pulse timing from the spinning frequency, or actively synchronizing the pulse scheme by feeding the spinning signal to the spectrometer. In both cases, even slight fluctuation of sample spinning causes huge  $t_1$  noise, which comes from the mismatch of rotor phases in two recoupling sequences for the former case and from the introduction of variable time delay for the latter case. This short-term stability cannot be evaluated by monitoring the frequency counter of MAS controller, which only shows the averaged frequency over much longer time period (100 ms to 1 s). The short-term stability is more important at faster MAS, since faster MAS amplifies the rotor phase deviation from the expected phase. For example, while the 1% deviation at 10 kHz MAS introduces only 0.1 rotation ( $=36^\circ$ ) of sample rotor after 1 ms, it results in 1 rotor ( $=360^\circ$ ) changes of rotor phase at 100 kHz. This is because the rotor spins 10 times within 1 ms at 10 kHz, on the other hand the sample rotor rotates 100 times during the same time period at 100 kHz MAS. It shows that 10 times more stable spinning at 100 kHz is required than 10 kHz MAS. The short-term fluctuations can be experimentally monitored by digital oscilloscopes. The oscilloscope is first triggered, and the signal is observed after several ms of triggering. The persistent display mode allows to monitor the fluctuation of sample spinning. If the sample spinning is perfectly stable, we should not see any fluctuation of the waveform. The fluctuations appear as a jitter on the screen. The picture shown in Fig. 6.8 is taken with 1 ms delayed trigger and shows  $\pm 0.5 \mu\text{s}$  variation, which corresponds to 250 ppm variation of MAS rate. Such level of stability is typically required in D-HMQC experiment. Note that the fluctuations that are obtained from MAS controller display should be in the range  $\pm 10$  Hz (140 ppm) and smaller than the short-term fluctuations. The very different short-term stability can be observed even with the same read of MAS controller, since the short- and long-term stability is partially independent on each other. This emphasizes the importance of checking the short-term stability by monitoring the oscilloscope when significant  $t_1$  noise appears in D-HMQC experiments.

The sample insertion to the stator can be problematic and time-consuming for very tiny rotors  $\sim 0.75$  mm, since the rotor can stick on the stator wall due to the electrostatic force. To check the proper insertion of the sample rotor in the MAS

**Fig. 6.8** Snapshot of the oscilloscope screen at 70 kHz MAS. The spinning signal is monitored after 1 ms trigger with the persistent mode. The jitter ( $\pm 0.5 \mu\text{s}$ ) represents the spinning fluctuations of 250 ppm



stator and hence to save time, it is advisable to use the oscilloscope. When the rotor is properly inserted into the stator, the spinning detector observes some signals, otherwise it gives no signal.

## 6.4 Setup of 2D Measurements

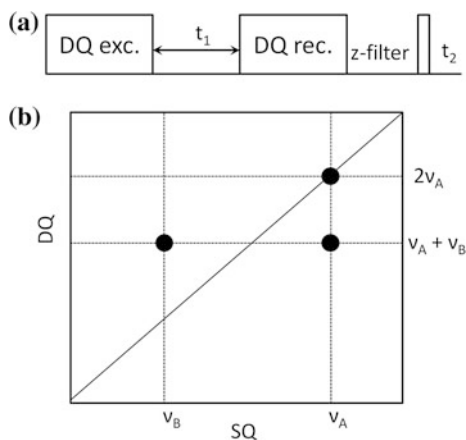
### 6.4.1 $^1\text{H}$ DQ/SQ Correlation

Homonuclear and heteronuclear correlation experiments are very informative experiments in NMR measurements. While the internuclear correlations are established using internuclear interactions, very fast MAS suppresses these interactions. Even though, using the residual interactions or reintroducing interactions by rf irradiations, the internuclear correlations can be easily made. At very fast MAS,  $^1\text{H}$ - $^1\text{H}$  correlation measurements are useful for practical applications because of high sensitivity and information content [17]. Since  $^1\text{H}$  is highly abundant nuclei with large gyromagnetic ratio, it is straightforward to obtain  $^1\text{H}$ - $^1\text{H}$  correlations. Moreover, since  $^1\text{H}$  is located on the surface of the molecules,  $^1\text{H}$ - $^1\text{H}$  correlations give insight into the intermolecular interactions in addition to intramolecular interactions. In particular,  $^1\text{H}$  DQ/SQ correlation is useful for such information. While the SQ/SQ experiments always give strong diagonal autocorrelation peaks in addition to cross-peaks, DQ/SQ experiments only give internuclear cross-peaks. The experiments and spectra are similar to INADEQUATE, which gives  $^{13}\text{C}$  DQ/SQ correlation through J-coupling. The major difference between  $^{13}\text{C}$  INADEQUATE and  $^1\text{H}$  DQ/SQ experiment is the interactions used to correlate nuclei. This results in different behavior at diagonal peaks; while J-based INQDEQUATE does not give any diagonal peak,  $^1\text{H}$  DQ/SQ experiment gives. The diagonal peak in  $^1\text{H}$  DQ/SQ spectra is direct evidence of proximity between

same kinds of nuclei. The schematic representations of DQ/SQ pulse sequence and correlation spectrum are shown in Fig. 6.9. First, the DQ coherence is prepared by the initial excitation block and then evolves during the  $t_1$  period. The resultant DQ coherence is back-transferred to the z magnetization by the reconversion block. The residual transversal coherence is removed either by the phase cycling or z-filtering. Finally, the magnetization is excited by the  $90^\circ$  pulse and observed during the  $t_2$  period. The Fourier transformation to both dimensions gives DQ/SQ correlation spectra. The cross-peak between two nuclei (A and B) appears along the SQ axis. While the DQ coherence evolves at the sum of two resonance frequencies,  $\nu_A + \nu_B$ , the SQ coherence thus obtained shows frequencies  $\nu_A$  and  $\nu_B$ . This results in the 2D correlations at (DQ, SQ) =  $(\nu_A + \nu_B, \nu_A)$  and  $(\nu_A + \nu_B, \nu_B)$ . These peaks appear symmetrically with respect to the diagonal line with a slope of 2. If two nuclei have the identical chemical shift, the correlation peak appears on the diagonal line at  $2\nu_A$ . The DQ/SQ spectrum in Fig. 6.9b shows the presence of (A, A) and (A, B) correlations and the absence of (B, B) correlations. It should be noted that the DQ/SQ correlation spectra not only give proximity between  $^1\text{H}$ s but also impart additional resolution, which is advantageous for practical applications.

The excitation and reconversion blocks can be comprehended by the first-order and higher-order average Hamiltonians [75–83]. The former includes back-to-back (BABA), symmetry-based pulses, while latter uses dipolar homonuclear homogeneous Hamiltonian ( $\text{DH}^3$ ) terms, which come from higher-order perturbations in the INADEQUATE sequence. The use of the first-order recoupling allows quick buildup and reconversion of DQ coherences, minimizing the relaxation decay during excitation/reconversion blocks. In addition, the dipolar truncation removes remote correlations, limiting the correlation for short-range ( $\sim 4 \text{ \AA}$ ) proximities. This feature is useful to understand the local  $^1\text{H}$ – $^1\text{H}$  network structures. The use of the first-order average Hamiltonian induces peak position shift/splitting at an integer multiple of the spinning frequency in the DQ dimension [84]. To avoid such complexity, the excitation and reconversion block should be exactly synchronized to the sample spinning; i.e., increments in the  $t_1$  dimension must be an integer

**Fig. 6.9** Schematic representation of  $^1\text{H}$  DQ/SQ pulse sequence (a) and spectrum (b)



multiple of the cycle time of the sample spinning. It is noteworthy that the requirement of the rotor synchronization of the  $t_1$  dimension induces  $t_1$  noise in the presence of spinning fluctuations. This can be avoided by utilizing the higher-order average Hamiltonian with the sequence exactly same as INADEQUATE. Although INADEQUATE requires only J-coupling, the  $DH^3$  terms can be used throughout the dipolar-based  $^1H$  network [75]. The use of the  $DH^3$  terms allows non-rotor-synchronous acquisition in the  $t_1$  dimension and, therefore, is less sensitive toward spinning fluctuations. However, the overall sensitivity in general is lower than that of the first-order recoupling sequences.

Here, we demonstrate the experimental setup of  $^1H$  DQ/SQ correlation measurements. BABA-xy16 [72] is recommended for the DQ recoupling sequence due to its high efficiency and robustness toward experimental imperfections. The cycle time of BABA-xy16 is  $8\tau_r$ , where  $\tau_r$  is the cycle time of sample spinning, and enough long to reach the plateau of buildup curve for  $^1H$ - $^1H$  homonuclear coupled systems. Thus, one cycle of BABA-xy16 can be safely used without any optimization. The only adjustable parameter is the  $90^\circ$  pulse width used in the BABA recoupling sequence. This is easily optimized by monitoring  $^1H$  DQ filtered spectra with varying pulse widths in the BABA recoupling, using the sequence shown in Fig. 6.9a with  $t_1 = 0$ . Although theoretically the optimal flip angle is  $90^\circ$ , the experimentally obtained maxima always appear at a pulse length shorter than the  $90^\circ$  pulse width. This is because of higher-order recoupling in the BABA sequences. This effect becomes smaller at faster MAS rate because it is higher-order effect; thus, the optimization should be done at every MAS rate. Since the spin system can also affect this phenomenon, it is advisable to optimize conditions for each sample. However, the dependence to samples is generally small for most organic molecules, and optimization can be skipped. The optimal  $90^\circ$  pulses used in the BABA sequences are typically found in the range of  $40^\circ$  to  $90^\circ$  pulse widths. DQ filtering efficiency can be evaluated by comparing the  $^1H$  single pulse spectrum and the DQ filtered spectrum. The efficiency is strongly dependent on sample and in general lies between 20 and 40% of the intensities of  $^1H$  single-pulse spectra. This allows quick measurements of  $^1H$  DQ/SQ correlation spectra with reasonable sensitivities. The measurement time is dominated by the number of  $t_1$  points and the phase cycling rather than the sensitivity because of the high efficiency. To minimize the indirect spectral points, thus experimental time, the  $^1H$  offset should be set to the center of the SQ  $^1H$  spectral width. The indirect spectral width should be larger than twice of the maximum  $^1H$  chemical shift separation in the SQ dimension and synchronized to the sample spinning. The number of phase cycling can be minimized to 4 for each  $t_1$  slice by z-filtering (typically 1 ms) for the coherence selection after the reconversion block. However, this procedure can introduce additional peaks due to spin diffusion during the z-filtering. This problem can be avoided by removing z-filtering with the additional phase cycling (at least 12 scans).

The experimental optimization is demonstrated on  $^{13}C_3, ^{15}N$  L-alanine at 70 kHz MAS (shown in Fig. 6.10). The maximum appears at  $0.56 \mu s$ , which is corresponding to  $44^\circ$  pulse length. The 2D DQ/SQ correlation spectrum of L-histidine·HCl·H<sub>2</sub>O is shown in Fig. 6.11. Since L-histidine·HCl·H<sub>2</sub>O is very small



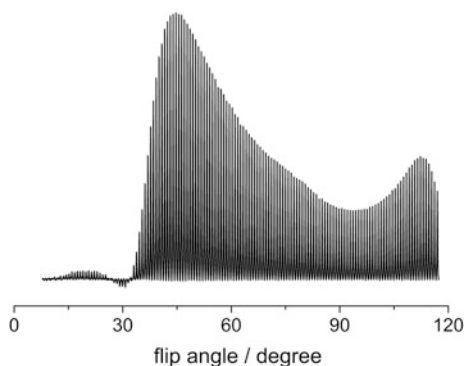


**Fig. 6.10**  $^1\text{H}$  DQ filtered spectra of  $^{13}\text{C}_3$ ,  $^{15}\text{N}$ , L-alanine at 70 MHz MAS under 14.1 T. BABA-xy16 of  $\tau_{\text{exc}} = \tau_{\text{rec}} = 114 \mu\text{s}$  with various flip angles is applied during excitation and reconversion period. The  $90^\circ$  pulse length measured from the first maxima is  $1.15 \mu\text{s}$  and used to calculate the flip angle

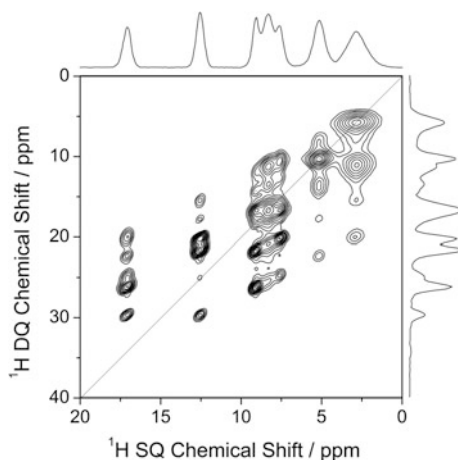


**Fig. 6.11**  $^1\text{H}$  DQ/SQ correlation spectrum of L-histidine-HCl· $\text{H}_2\text{O}$  under 70 kHz MAS at 14.1 T using BABA-xy16 recoupling sequence with  $\tau_{\text{exc}} = \tau_{\text{rec}} = 114 \mu\text{s}$ . z-filter was not applied to avoid unwanted spin diffusion and 12 scans are collected with the phase cycling to select the proper coherence pathway. While the pulse length in the BABA sequence is optimized to  $0.56 \mu\text{s}$ , the  $90^\circ$  pulse length of  $1.15 \mu\text{s}$ , which is obtained from the first maxima of  $^1\text{H}$  nutation curve, is used for the excitation pulse just before the signal acquisition. The indirect spectral width is set to 35 kHz so that the  $t_1$  evolution time and two BABA sequences are synchronized to sample spinning. 64 hypercomplex  $t_1$  points are collected using the states-TPPI approach. The total acquisition time is 2.1 h with a repetition delay of 5 s

molecule, most of the possible  $^1\text{H}$ - $^1\text{H}$  correlations are observed except for auto-correlation of NH at (DQ, SQ) = (34.2 ppm, 17.1 ppm). It is interesting to see the very weak intermolecular autocorrelation between NHs ( $4.8 \text{ \AA}$  apart) at (DQ, SQ) = (25.0 ppm, 12.5 ppm).

## 6.4.2 $^1\text{H}$ -detected $^1\text{H}/\text{X}$ CP-HSQC

Very fast MAS dramatically improves the efficiency of  $^1\text{H}$  indirectly detected heteronuclear correlation (idHETCOR) experiments on rigid solids [7–16]. The  $^1\text{H}$  indirect observation is widely used as sensitivity enhancement methods in solution NMR. In the  $^1\text{H}$  indirect detection scheme, first,  $^1\text{H}$  magnetization is transferred to X nuclei, followed by the time evolution of X magnetization. Finally, X magnetization is back-transferred to  $^1\text{H}$  for detection. The sensitivity in  $^1\text{H}$  indirect detection is basically independent to the gyromagnetic ratio of X nuclei; thus, the sensitivity enhancement factor is greatly improved for low gamma X nuclei as

$$\frac{\text{SNR}_{\text{indirect}}}{\text{SNR}_{\text{direct}}} = f \left( \frac{\Delta_{\text{X}}}{\Delta_{\text{H}}} \right) \left( \frac{\gamma_{\text{H}}}{\gamma_{\text{X}}} \right)^{3/2} \quad (6.1)$$

where  $f$  is various experimental factors including probe Q factors, magnetization transfer efficiency,  $\Delta_{\text{X(H)}}$  and  $\gamma_{\text{X(H)}}$  are apparent linewidth in the X ( $^1\text{H}$ ) dimension and gyromagnetic ratio of X ( $^1\text{H}$ ), respectively [7]. This equation well illustrates the necessity of the very fast MAS in rigid solids as the  $^1\text{H}$  linewidth due to  $^1\text{H}$ – $^1\text{H}$  dipolar interactions is inversely proportional to the MAS frequency. It also avoids the difficulty associated with probe ringing, which is more prevalent in the case of quadrupolar nuclei. In addition, the folding of spinning sideband in solid-state MAS NMR with the rotor-synchronized  $t_1$  acquisition enhances the sensitivity along with removal of spinning sidebands in systems with large anisotropies. The sequence includes two-way magnetization transfer of  $^1\text{H} \rightarrow \text{X} \rightarrow ^1\text{H}$ . There are several different mechanisms of magnetization transfer including CP, refocused-INEPT, J/D-HMQC and complete list can be found in the literature [35]. X nucleus can be either spin-1/2 or quadrupolar nuclei including  $^{14}\text{N}$ . When X is spin-1/2 nuclei, e.g.,  $^{13}\text{C}$  and  $^{15}\text{N}$ , indirect detection HETCOR (HSQC) approaches are useful because  $^1\text{H}$  decoupling can be applied during the  $t_1$  period. In the CP-HSQC pulse sequence, the first  $^1\text{H} \rightarrow \text{X}$  transfer is achieved by CP while the second  $\text{X} \rightarrow ^1\text{H}$  transfer can be achieved either by CP or refocused-INEPT [15]. Basically, CP and refocused-INEPT transfer gives through-space and bond correlation, respectively. However, both CP and refocused-INEPT give similar results if the contact time of the second CP is sufficiently short at the very fast MAS conditions. This results in pseudo through-bond correlation even with CP for both magnetization transfers [47]. For the simplicity of experimental setup, we here focus on CP/CP-HSQC experiments, where CP is utilized for both  $^1\text{H} \rightarrow \text{X}$  and  $\text{X} \rightarrow ^1\text{H}$  magnetization transfers (Fig. 6.12). First, X magnetization is prepared by the first CP from the  $^1\text{H}$  magnetization followed by the time evolution under  $^1\text{H}$  decoupling during the  $t_1$  period. The X transversal magnetization is stored along the z-axis to halt the time evolution. The residual  $^1\text{H}$  magnetization is suppressed by the HORROR  $^1\text{H}$ – $^1\text{H}$  recoupling [85]. This irradiation also removes residual solvent signals if present [86]. Finally, the X magnetization is back-transferred to  $^1\text{H}$  by the second  $\text{X} \rightarrow ^1\text{H}$  CP followed by the  $^1\text{H}$  observation under the X decoupling during

**Fig. 6.12** Schematic representation of  $^1\text{H}/\text{X}$  CP/CP-HSQC correlation measurements

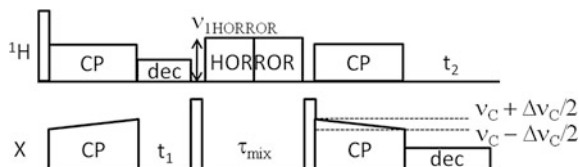


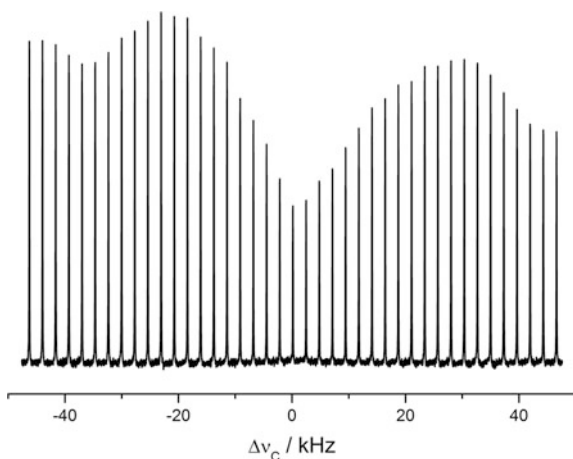
**Table 6.2** Building blocks in the CP/CP-HSQC experiments with optimization strategy

Blocks	Optimization
CPs	Standard sample (contact time can be optimized with the sample of interest)
HORROR	Sample of interest
X decoupling	Standard sample
$^1\text{H}$ decoupling	Standard sample

the  $t_2$  period. Even if X is a rare nucleus, X decoupling is mandatory because  $^1\text{H}$  nucleus observed in this sequence always accompanies the X nucleus. Each building blocks used in the sequence can be optimized separately by using standard samples (Table 6.2) as well as sample of interest.

$^{13}\text{C}_3$ ,  $^{15}\text{N}$  L-alanine can be used as a standard sample to set up experimental conditions. The HORROR condition can be roughly calculated by setting the rf field strength equal to  $v_R/2$  and fine optimization is achieved by minimizing the residual signal after spinlock (1–5 ms). The HORROR duration for natural abundance samples can be long (20–100 ms) to suppress the residual signal and, however, cannot be longer than the  $t_1$  relaxation time of X to avoid signal loss due to longitudinal relaxation. The CP conditions are roughly adjusted by  $^{13}\text{C}$  CPMAS. The shaped CP schemes are recommended to maximize the efficiency. While RAMP CP on the  $^{13}\text{C}$  channel can be recommended for simplicity [87], other schemes like tangential CP can be used alternatively. The RAMP on  $^1\text{H}$  instead of  $^{13}\text{C}$  can also be used without significant difference in efficiency after proper optimizations. It should be noted that unlike moderate MAS CP conditions, the sense of RAMP greatly affects the magnetization transfer efficiency and should be optimized (Fig. 6.13). In this example,  $^{13}\text{C}$  rf field strength  $v_C$  is linearly varied from  $v_C - \Delta v_C/2$  to  $v_C + \Delta v_C/2$  and the optimal condition is found at the negative ramp (descending rf field strength) with  $\Delta v_C = -23$  kHz. Indeed, the signal intensity at  $\Delta v_C = 23$  kHz gives only ca 80% of the maximum at  $\Delta v_C = -23$  kHz. Very fast MAS allows to use low power CP conditions. A great care must be taken to avoid any recoupling conditions. The DQ CP ( $n = 1$ ) condition [88] with  $v_C \sim 2v_R/3$  and  $v_H \sim v_R/3$  is generally recommended to cover the wider  $^{13}\text{C}$  chemical shift range than  $^1\text{H}$ . The fine optimization should be done by monitoring  $^1\text{H} \rightarrow ^{13}\text{C} \rightarrow ^1\text{H}$  1D CP/CP-HSQC signal intensities. Although the contact time of two CP transfers can be different, the symmetric RAMP CP generally gives the best efficiency from our personal experience; the positive ramp on the first CP and negative ramp on the

**Fig. 6.13**  $^{13}\text{C}$  CPMAS signal intensities of the CH moiety of  $^{13}\text{C}_3$ ,  $^{15}\text{N}$  L-alanine with various  $\Delta\nu_{\text{C}}$ . The rf fields of  $\nu_{\text{C}} = 51$  kHz and  $\nu_{\text{H}} = 19$  kHz are used



second CP, and vice versa. This is most probably due to the time-reversible behavior of spin systems. While the contact time of the first CP is typically 1–2 ms, that of the second CP can be 0.3–0.5 ms. Even with such a short second CP, the efficient magnetization transfer is achieved due to dipolar truncation effect. The longer contact time of the second CP may introduce remote  $^1\text{H}$ – $^{13}\text{C}$  correlations and should be avoided if pseudo through-bond correlations are needed. Both  $^1\text{H}$  and  $^{13}\text{C}$  decoupling can be performed by WALTZ at 10 kHz rf field strength without further optimization [89]. While the two-way  $^1\text{H} \rightarrow ^{13}\text{C} \rightarrow ^1\text{H}$  magnetization efficiency of the CH moiety of  $^{13}\text{C}_3$ ,  $^{15}\text{N}$  L-alanine is about 30–40%; it can be improved in the natural abundance samples.

## 6.5 Conclusions

In this chapter, the practical hands-on guides for setups of the fast MAS experiments are presented. While very fast MAS probes offer an attractive set of experiments for structural analysis at the atomic scale, those also require careful setup of experimental conditions compared to the moderate MAS rate probes. First, sample-independent factors are discussed including shimming, magic-angle adjustment, rf field strength calibrations, and referencing. It is discussed how to overcome the difficulties associated with the weak signal intensity due to the limited sample volume, very short pulses, etc. The discussions on sample-dependent factors such as relaxation delay and spinning fluctuations are followed.  $^1\text{H}$  relaxation times are no longer uniform at very fast MAS rate and special care must be taken to set up the repetition delay. The spinning fluctuations can be critical factor to reduce the  $t_1$  noise in rotor-synchronous experiments and should be monitored by oscilloscopes. Finally, two practically useful homonuclear and heteronuclear correlation experiments are introduced together with experimental setups.

In spite of the limited sample volume,  $^1\text{H}$  indirectly detected heteronuclear experiments and  $^1\text{H}/^1\text{H}$  homonuclear correlation experiments achieve high-throughput solid-state NMR measurements at very fast MAS rate. I believe the application of very fast MAS will spread very quickly and widely, and enhance the ability of solid-state NMR in various applications. I am hoping this chapter will help these improvements.

**Acknowledgements** We thank Dr. Manoj Kumar Pandey of Indian Institute of Technology Ropar for careful reading of the manuscript and helpful discussions.

## References

1. Schmidt-Rohr, K., Spiess, H.W.: *Multidimensional Solid-State NMR and Polymers*. Academic Press, London (1994)
2. Livitt M.H.: *Spin Dynamics*, 2 edn. Wiley, London (2008)
3. Andrew, E.R., Bradbury, A., Eades, R.G.: Nuclear magnetic resonance spectra from a crystal rotated at high speed. *Nature* **182**, 1659 (1958)
4. Lowe, I.J.: Free induction decays of rotating solids. *Phys. Rev. Lett.* **2**, 285 (1959)
5. Zorin, V.E., Brown, S.P., Hodgkinson, P.: Origins of line width in  $^1\text{H}$  magic-angle spinning NMR. *J. Chem. Phys.* **125**, 144508 (2006)
6. Brunner, E., Freude, D., Gerstein, B.C., Pfeifer, H.: Residual linewidths of NMR spectra of spin-1/2 systems under magic-angle spinning. *J. Magn. Reson.* **90**, 90–99 (1990)
7. Ishii, Y., Tycko, R.: Sensitivity enhancement in solid state  $^{15}\text{N}$  NMR by indirect detection with high-speed magic angle spinning. *J. Magn. Reson.* **142**, 199–204 (2000)
8. Ishii, Y., Yesinowski, J.P., Tycko, R.: Sensitivity enhancement in solid-state  $^{13}\text{C}$  NMR of synthetic polymers and biopolymers by  $^1\text{H}$  NMR detection with high-speed magic angle spinning. *J. Am. Chem. Soc.* **123**, 2921–2922 (2001)
9. Paulson, E.K., Morcombe, C.R., Gaponenko, V., Dancheck, B., Byrd, R.A., Zilm, K.W.: Sensitive high resolution inverse detection NMR spectroscopy of proteins in the solid-state. *J. Am. Chem. Soc.* **125**, 15831–15836 (2003)
10. Reif, B., Griffin, R.G.:  $^1\text{H}$  detected  $^1\text{H}$ ,  $^{15}\text{N}$  correlation spectroscopy in rotating solids. *J. Magn. Reson.* **160**, 78–83 (2003)
11. Zhou, D.H., Rienstra, C.M.: Rapid analysis of organic compounds by proton-detected heteronuclear correlation NMR spectroscopy with 40 kHz magic-angle spinning. *Angew. Chem. Int. Ed.* **47**, 7328–7331 (2008)
12. Zhou, D.H., Shah, G., Cormos, M., Mullen, C., Sandoz, D., Rienstra, C.M.: Proton-detected solid-state NMR spectroscopy of fully protonated proteins at 40 kHz magic-angle spinning. *J. Am. Chem. Soc.* **129**, 11791–11801 (2007)
13. Zhou, D.H., Shea, J.J., Nieuwkoop, A., Franks, W.T., Wylie, B.J., Mullen, C., Sandoz, D., Rienstra, C.M.: Solid state protein structure determination with proton detected triple resonance 3D magic angle spinning NMR spectroscopy. *Angew. Chem. Int. Ed.* **46**, 8380–8383 (2007)
14. Wiench, J.W., Bronnimann, C.E., Lin, V.S.-Y., Pruski, M.: Chemical shift correlation NMR spectroscopy with indirect detection in fast rotating solids: studies of organically functionalized mesoporous silicas. *J. Am. Chem. Soc.* **129**, 12076–12077 (2007)
15. Mao, K., Pruski, M.: Directly and indirectly detected through-bond heteronuclear correlation solid-state NMR spectroscopy under fast MAS. *J. Magn. Reson.* **201**, 165–174 (2009)

16. Althaus, S.M., Mao, K., Stringer, J.A., Kobayashi, T., Pruski, M.: Indirectly detected heteronuclear correlation solid-state NMR spectroscopy of naturally abundant  $^{15}\text{N}$  nuclei. *Solid State Nucl. Magn. Reson.* **57–58**, 17–21 (2014)
17. Ishii, Y., Wickramasinghe, N.P., Chimon, S.: A new approach in 1D and 2D  $^{13}\text{C}$  high-resolution solid-state NMR spectroscopy of paramagnetic organometallic complexes by very fast magic-angle spinning. *J. Am. Chem. Soc.* **125**, 3438–3439 (2003)
18. Wickramasinghe, N.P., Shaibat, M., Ishii, Y.: Enhanced sensitivity and resolution in  $^1\text{H}$  solid-state NMR spectroscopy of paramagnetic complexes under very fast magic angle spinning. *J. Am. Chem. Soc.* **127**, 5796–5797 (2005)
19. Wickramasinghe, N.P., Shaibat, M.A., Jones, C.R., Casabianca, L.B., de Dios, A.C., Harwood, J.S., Ishii, Y.: Progress in  $^{13}\text{C}$  and  $^1\text{H}$  solid-state nuclear magnetic resonance for paramagnetic systems under very fast magic angle spinning. *J. Chem. Phys.* **128**, 052210 (2008)
20. Parthasarathy, S., Nishiyama, Y., Ishii, Y.: Sensitivity and resolution enhanced solid-state NMR for paramagnetic systems and biomolecules under very fast magic angle spinning. *Acc. Chem. Res.* **46**, 2127–2135 (2013)
21. Shen, M., Trebosc, J., Lafon, O., Gan, Z.H., Pourpoint, F., Hu, B.W., Chen, Q., Amoureux, J. P.: Solid-state NMR indirect detection of nuclei experiencing large anisotropic interactions using spinning sideband-selective pulses. *Solid State Nucl. Magn. Reson.* **72**, 104–117 (2015)
22. Pöppler, A.-C., Demers, J.-P., Malon, M., Singh, A.P., Roesky, H.W., Nishiyama, Y., Lange, A.: Ultra-fast magic angle spinning: benefits for the acquisition of ultra-wideline NMR spectra of heavy spin-1/2 nuclei. *ChemPhysChem* **17**, 812–816 (2016)
23. Rossini, A.J., Hanrahan, M.P., Thuo, M.: Rapid acquisition of wideline MAS solid-state NMR spectra with fast MAS, proton detection, and dipolar HMQC pulse sequences. *Phys. Chem. Chem. Phys.* **18**, 25284–25295 (2016)
24. Samoson, A., Tuherm, T., Gan, Z.: High-field high-speed MAS resolution enhancement in  $^1\text{H}$  NMR spectroscopy of solids. *Solid State Nucl. Magn. Reson.* **20**, 130–136 (2001)
25. Deschamps, M.: Ultrafast magic angle spinning nuclear magnetic resonance. *Annu. Rep. NMR Spectrosc.* **81**, 109–144 (2014)
26. Brown, S.P.: Probing proton–proton proximities in the solid state. *Prog. Nucl. Magn. Reson. Spectrosc.* **50**, 199–251 (2007)
27. Samoson, A., Tuherm, T., Past, J., Reinhold, A., Heinmaa, I., Anupöld, T., Smith, M.E., Pike, K.J.: Fast Magic-Angle Spinning: Implications, *Encyclopedia of Magnetic Resonance*, pp. 1–20. Wiley, Chichester (2010)
28. Samoson, A.: Magic-angle spinning extensions. In: Harris, R.K., Grant, D.M. (eds.) *Encyclopedia of Nuclear Magnetic Resonance*, pp. 59–64. Wiley, Chichester (2002)
29. Zhou, D.H.: Fast Magic Angle Spinning for Protein Solid-State NMR Spectroscopy, *Encyclopedia of Magnetic Resonance*, pp. 331–342. Wiley, Chichester (2007)
30. Brown, S.P.: Applications of high-resolution  $^1\text{H}$  solid-state NMR. *Solid State Nucl. Magn. Reson.* **41**, 1–27 (2012)
31. Demers, J.-P., Chevelkov, V., Lange, A.: Progress in correlation spectroscopy at ultra-fast magic-angle spinning: Basic building blocks and complex experiments for the study of protein structure and dynamics. *Solid State Nucl. Magn. Reson.* **40**, 101–113 (2011)
32. Hodgkinson, P.: High-resolution  $^1\text{H}$  NMR spectroscopy of solids. *Annu. Rep. NMR Spectrosc.* **72**, 185 (2011)
33. Su, Y.C., Andreas, L., Griffin, R.G.: In: Kornberg, R.D. (ed) *Annual Review of Biochemistry*, vol. 84, pp. 465–497 (2015)
34. Mote, K.R., Madhu, P.K.: Proton-detected solid-state NMR spectroscopy of fully protonated proteins at slow to moderate magic-angle spinning frequencies. *J. Magn. Reson.* **261**, 149–156 (2015)
35. Nishiyama, Y.: Fast magic-angle sample spinning solid-state NMR at 60–100 kHz for natural abundance samples. *Solid State Nucl. Magn. Reson.* **78**, 24–36 (2016)
36. Kobayashi, T., Mao, K., Paluch, P., Nowak-Krol, A., Sniechowska, J., Nishiyama, Y., Gryko, D.T., Potrzebowski, M.J., Pruski, M.: Study of intermolecular interactions in the corrole

- matrix by solid-state NMR under 100 kHz MAS and theoretical calculations. *Angew. Chem. Int. Ed.* **52**, 14108–14111 (2013)
37. Agarwal, V., Penzel, S., Szekely, K., Cadalbert, R., Testori, E., Oss, A., Past, J., Samoson, A., Ernst, M., Bockmann, A., Meier, B.H.: De novo 3D structure determination from sub-milligram protein samples by solid-state 100 kHz MAS NMR spectroscopy. *Angew. Chem. Int. Ed.* **53**, 12253–12256 (2014)
  38. Zhou, D.H., Shea, J.J., Nieuwkoop, A.J., Franks, W.T., Wylie, B.J., Mullen, C., Sandoz, D., Rienstra, C.M.: Solid-state protein-structure determination with proton-detected triple-resonance 3D magic-angle-spinning NMR spectroscopy. *Angew. Chem. Int. Ed.* **46**, 8380–8383 (2007)
  39. Barbet-Massin, E., Pell, A.J., Retel, J.S., Andreas, L.B., Jaudzems, K., Franks, W.T., Nieuwkoop, A.J., Hiller, M., Higman, V., Guerry, P., Bertarello, A., Knight, M.J., Felletti, M., Le Marchand, T., Kotelovica, S., Akopjana, I., Tars, K., Stoppini, M., Bellotti, V., Bolognesi, M., Ricagno, S., Chou, J.J., Griffin, R.G., Oschkinat, H., Lesage, A., Emsley, L., Herrmann, T., Pintacuda, G.: Rapid proton-detected NMR assignment for proteins with fast magic angle spinning. *J. Am. Chem. Soc.* **136**, 12489–12497 (2014)
  40. Penzel, S., Smith, A.A., Agarwal, V., Hunkeler, A., Org, M.L., Samoson, A., Bockmann, A., Ernst, M., Meier, B.H.: Protein resonance assignment at MAS frequencies approaching 100 kHz: a quantitative comparison of J-coupling and dipolar-coupling-based transfer methods. *J. Biomol. NMR* **63**, 165–186 (2015)
  41. Lafon, O., Wang, Q., Hu, B.W., Vasconcelos, F., Trebosc, J., Cristol, S., Deng, F., Amoureux, J.-P.: Indirect detection via spin-1/2 nuclei in solid state NMR spectroscopy: application to the observation of proximities between protons and quadrupolar nuclei. *J. Phys. Chem. A* **113**, 12864–12878 (2009)
  42. Hung, I., Zhou, L.N., Pourpoint, F., Grey, C.P., Gan, Z.: Isotropic high field NMR spectra of Li-Ion battery materials with anisotropy >1 MHz. *J. Am. Chem. Soc.* **134**, 1898–1901 (2012)
  43. Gan, Z., Amoureux, J.-P., Trebosc, J.: Proton-detected <sup>14</sup>N MAS NMR using homonuclear decoupled rotary resonance. *Chem. Phys. Lett.* **435**, 163–169 (2007)
  44. Cavadini, S., Abraham, A., Bodenhausen, G.: Proton-detected nitrogen-14 NMR by recoupling of heteronuclear dipolar interactions using symmetry-based sequences. *Chem. Phys. Lett.* **445**, 1–5 (2007)
  45. Wiench, J.W., Bronnimann, C.E., Lin, V.S.Y., Pruski, M.: Chemical shift correlation NMR spectroscopy with indirect detection in fast rotating solids: studies of organically functionalized mesoporous silicas. *J. Am. Chem. Soc.* **129**, 12076–12077 (2007)
  46. Nishiyama, Y., Kobayashi, T., Malon, M., Singappuli-Arachchige II, D., Slowing, M., Pruski: Studies of minute quantities of natural abundance molecules using 2D heteronuclear correlation spectroscopy under 100 kHz MAS. *Solid State Nucl. Magn. Reson.* **66–67**, 56–61 (2015)
  47. Shishovs, M., Rumnieks, J., Diebolder, C., Jaudzems, K., Andreas, L.B., Stanek, J., Kazaks, A., Kotelovica, S., Akopjana, I., Pintacuda, G., Koning, R.I., Tars, K.: Structure of AP205 coat protein reveals circular permutation in ssRNA bacteriophages. *J. Mol. Biol.* **428**, 4267–4279 (2016)
  48. Ernst, M., Samoson, A., Meier, B.H.: Low-power decoupling in fast magic-angle spinning NMR. *Chem. Phys. Lett.* **348**, 293–302 (2001)
  49. Ernst, M., Samoson, A., Meier, B.H.: Low-power XiX decoupling in MAS NMR experiments. *J. Magn. Reson.* **163**, 332–339 (2003)
  50. Kotecha, M., Wickramasinghe, N.P., Ishii, Y.: Efficient low-power heteronuclear decoupling in <sup>13</sup>C high-resolution solid-state NMR under fast magic angle spinning. *Magn. Reson. Chem.* **45**, S221–S230 (2007)
  51. Lange, A., Scholz, I., Manolikas, T., Ernst, M., Meier, B.H.: Low-power cross polarization in fast magic-angle spinning NMR experiments. *Chem. Phys. Lett.* **468**, 100–105 (2009)
  52. Vijayan, V., Demers, J.-P., Biernat, J., Mandelkow, E., Becker, S., Lange, A.: Low-power solid-state NMR experiments for resonance assignment under fast magic-angle spinning. *ChemPhysChem* **10**, 2205–2208 (2009)

53. Romeo, F., Hoult, D.I.: Magnetic field profiling: analysis and correcting coil design. *Magn. Reson. Med.* **1**, 4–65 (1984)
54. Prammer, M.G., Haselgrove, J.C., Shinnar, M., Leigh, J.S.: A new approach to automatic shimming. *J. Magn. Reson.* **77**, 40–52 (1988)
55. Barjat, H., Chilvers, P.B., Fetler, B.K., Horne, T.J., Morris, G.A.: A practical method for automated shimming with normal spectrometer hardware. *J. Magn. Reson.* **125**, 197–201 (1997)
56. van Zijl, P.C.M., Sukumar, S., O’Neil Johnson, M., Webb, P., Hurd, R.E.: Optimized shimming for high-resolution NMR using three-dimensional image-based field mapping. *J. Magn. Reson. A* **111**, 203–207 (1994)
57. Vanderhart, D.L., William, L., Garroway, A.N.: Resolution in  $^{13}\text{C}$  NMR of organic solids using high-power proton decoupling and magic-angle sample spinning. *J. Magn. Reson.* **44**, 361–401 (1981)
58. Kubo, A., Spaniol, T.P., Terao, T.: The effect of bulk magnetic susceptibility on solid state NMR spectra of paramagnetic compounds. *J. Magn. Reson.* **133**, 330–340 (1998)
59. Elbayed, K., Bourdonneau, M., Furrer, J., Richert, T., Raya, J., Hirsching, J., Piotto, M.: Origin of the residual NMR linewidth of a peptide bound to a resin under magic angle spinning. *J. Magn. Reson.* **136**, 127–129 (1999)
60. Nishiyama, Y., Tsutsumi, Y., Utsumi, H.: MAGIC SHIMMING: gradient shimming under magic angle sample spinning. *J. Magn. Reson.* **216**, 197–200 (2012)
61. Sodickson, A., Cory, D.G.: Shimming a high-resolution MAS probe. *J. Magn. Reson.* **128**, 87–91 (1997)
62. Piotto, M., Elbayed, K., Wieruszkeski, J.-M., Lippens, G.: Practical aspects of shimming a high resolution magic angle spinning probe. *J. Magn. Reson.* **173**, 84–89 (2005)
63. Frye, J.S., Maciel, G.E.: Setting the magic angle using a quadrupolar nuclide. *J. Magn. Reson.* **48**, 125–131 (1982)
64. Hayashi, S., Hayamizu, K.: Chemical shift standards in high-resolution solid-state NMR (1)  $^{13}\text{C}$ ,  $^{29}\text{Si}$ , and  $^1\text{H}$  nuclei. *Bull. Chem. Soc. Jpn.* **64**, 685–687 (1991)
65. Bertani, P., Raya, J., Bechinger, B.:  $^{15}\text{N}$  chemical shift referencing in solid state NMR. *Solid State Nucl. Magn. Reson.* **61–62**, 15–18 (2014)
66. Morcombe, C.R., Zilm, K.W.: Chemical shift referencing in MAS solid state NMR. *J. Magn. Reson.* **162**, 479–486 (2003)
67. Nishiyama, Y., Frey, M.H., Mukasa, S., Utsumi, H.:  $^{13}\text{C}$  solid-state NMR chromatography by magic angle spinning  $^1\text{H}$  T1 relaxation ordered spectroscopy. *J. Magn. Reson.* **202**, 135–139 (2010)
68. Ye, Y.Q., Malon, M., Martineau, C., Taulelle, F., Nishiyama, Y.: Rapid measurement of multidimensional  $^1\text{H}$  solid-state NMR Spectra at ultra-fast MAS frequencies. *J. Magn. Reson.* **239**, 75–80 (2014)
69. Nishiyama, Y., Zhang, R., Ramamoorthy, A.: Finite-pulse radio frequency-driven recoupling with phase cycling for 2D  $^1\text{H}/^1\text{H}$  correlation at ultrafast MAS frequencies. *J. Magn. Reson.* **243**, 25–32 (2014)
70. Lafon, O., Wang, Q., Hu, B., Vasconcelos, F., Trébosc, J., Cristol, S., Deng, F., Amoureux, J.-P.: Indirect detection via spin-1/2 nuclei in solid state NMR spectroscopy: application to the observation of proximities between protons and quadrupolar nuclei. *J. Phys. Chem. A* **113**, 12864–12878 (2009)
71. Tricot, G., Trébosc, J., Pourpoint, F., Gauvin, R., Delevoye, L.: The D-HMQC MAS-NMR technique: an efficient tool for the editing of through-space correlation spectra between quadrupolar and spin-1/2 ( $^3\text{1P}$ ,  $^{29}\text{Si}$ ,  $^1\text{H}$ ,  $^{13}\text{C}$ ) Nuclei. *Annu. Rep. NMR Spectrosc.* **81**, 145–184 (2014)
72. Gan, Z., Amoureux, J.-P., Trébosc, J.: Proton-detected  $^{14}\text{N}$  MAS NMR using homonuclear decoupled rotary resonance. *Chem. Phys. Lett.* **435**, 163–169 (2007)
73. Cavadini, S., Abraham, A., Bodenhausen, G.: Proton-detected nitrogen-14 NMR by recoupling of heteronuclear dipolar interactions using symmetry-based sequences. *Chem. Phys. Lett.* **445**, 1–5 (2007)



74. Nishiyama, Y., Endo, Y., Nemoto, T., Utsumi, H., Yamauchi, K., Hioka, K., Asakura, T.: Very fast magic angle spinning  $1\text{H}$ – $14\text{N}$  2D solid-state NMR: submicro-liter sample data collection in a few minutes. *J. Magn. Reson.* **208**, 44–48 (2011)
75. Feike, M., Demco, D.E., Graf, R., Gottwald, J., Hafner, S., Spiess, H.W.: Broadband multiple-quantum NMR spectroscopy. *J. Magn. Reson. A* **122**, 214–221 (1996)
76. Schnell, I., Spiess, H.W.: High-resolution  $1\text{H}$  NMR spectroscopy in the solid state: very-fast sample rotation and multiple-quantum coherences. *J. Magn. Reson./Adv. Magn. Reson.* **151**, 153–227 (2001)
77. Carravetta, M., Edén, M., Zhao, X., Brinkmann, A., Levitt, M.H.: Symmetry principles for the design of radiofrequency pulse sequences in the nuclear magnetic resonance of rotating solids. *Chem. Phys. Lett.* **321**, 205–215 (2000)
78. Levitt, M.H.: Symmetry-based pulse sequences in magic-angle spinning solid state NMR. In: Grant, D.M., Harris, R.K. (eds.) *Encyclopedia of Magnetic Resonance*, vol. 9, pp. 165–196. Wiley, Chichester (2002)
79. Brown, S.P., Spiess, H.W.: Advanced solid-state NMR methods for the elucidation of structure and dynamics of molecular, macromolecular, and supramolecular systems. *Chem. Rev.* **101**, 4125–4155 (2001)
80. Saalwächter, K., Lange, F., Matyjaszewski, K., Huang, C.-F., Graf, R.: BaBa-xy16: robust and broadband homonuclear DQ recoupling for applications in rigid and soft solids up to the highest MAS frequencies. *J. Magn. Reson.* **212**, 204–215 (2011)
81. Hu, B., Wang, Q., Lafon, O., Trébosc, J., Deng, F., Amoureux, J.P.: Robust and efficient spin-locked symmetry-based double-quantum homonuclear dipolar recoupling for probing  $1\text{H}$ – $1\text{H}$  proximity in the solid-state. *J. Magn. Reson.* **198**, 41–48 (2009)
82. Wang, Q., Hu, B., Lafon, O., Trébosc, J., Deng, F., Amoureux, J.-P.: Homonuclear dipolar recoupling under ultra-fast magic-angle spinning: Probing  $19\text{F}$ – $19\text{F}$  proximities by solid-state NMR. *J. Magn. Reson.* **203**, 113–128 (2010)
83. Deschamps, M., Fayon, F., Cadars, S., Rollet, A.-L., Massiot, D.:  $1\text{H}$  and  $19\text{F}$  ultra-fast MAS double-quantum single-quantum NMR correlation experiments using three-spin terms of the dipolar homonuclear Hamiltonian. *Phys. Chem. Chem. Phys.* **13**, 8024–8030 (2011)
84. Geen, H., Titman, J.J., Gottwald, J., Spiess, H.W.: Spinning sidebands in the fast-MAS multiple-quantum spectra of protons in solids. *J. Magn. Reson. A* **114**, 264–267 (1995)
85. Nielsen, N.C., Bildsøe, H., Jakobsen, H.J., Levitt, M.H.: Double-quantum homonuclear rotary resonance: Efficient dipolar recovery in magic-angle spinning nuclear magnetic resonance. *J. Chem. Phys.* **101**, 1805 (1994)
86. Zhou, D.H., Rienstra, C.M.: High-performance solvent suppression for proton detected solid-state NMR. *J. Magn. Reson.* **192**, 167–172 (2008)
87. Metz, G., Wu, X., Smith, S.O.: Ramped-amplitude cross polarization in magic-angle-spinning NMR. *J. Magn. Reson. A* **110**, 219–227 (1994)
88. Laage, S., Sachleben, J.R., Steuernagel, S., Pierattelli, R., Pintacuda, G., Emsley, L.: Fast acquisition of multi-dimensional spectra in solid-state NMR enabled by ultra-fast MAS. *J. Magn. Reson.* **196**, 133–141 (2009)
89. Wickramasinghe, A., Wang, S., Matsuda, I., Nishiyama, Y., Nemoto, T., Endo, Y., Ishii, Y.: Evolution of CPMAS under fast magic-angle-spinning at 100 kHz and beyond. *Solid State Nucl. Magn. Reson.* **72**, 9–16 (2015)